

# Superfluid stiffness of twisted trilayer graphene superconductors

<https://doi.org/10.1038/s41586-024-08444-3>

Received: 19 June 2024

Accepted: 22 November 2024

Published online: 5 February 2025

 Check for updates

Abhishek Banerjee<sup>1,7</sup>, Zeyu Hao<sup>1,7</sup>, Mary Kreidel<sup>1,7</sup>, Patrick Ledwith<sup>1</sup>, Isabelle Phinney<sup>1</sup>, Jeong Min Park<sup>2</sup>, Andrew Zimmerman<sup>1</sup>, Marie E. Wesson<sup>1</sup>, Kenji Watanabe<sup>3</sup>, Takashi Taniguchi<sup>4</sup>, Robert M. Westervelt<sup>1</sup>, Amir Yacoby<sup>1</sup>, Pablo Jarillo-Herrero<sup>2</sup>, Pavel A. Volkov<sup>1,5</sup>, Ashvin Vishwanath<sup>1</sup>, Kin Chung Fong<sup>6</sup>✉ & Philip Kim<sup>1</sup>✉

The robustness of the macroscopic quantum nature of a superconductor can be characterized by the superfluid stiffness,  $\rho_s$ , a quantity that describes the energy required to vary the phase of the macroscopic quantum wavefunction. In unconventional superconductors, such as cuprates, the low-temperature behaviour of  $\rho_s$  markedly differs from that of conventional superconductors owing to quasiparticle excitations from gapless points (nodes) in momentum space. Intensive research on the recently discovered magic-angle twisted graphene family has revealed, in addition to superconducting states, strongly correlated electronic states associated with spontaneously broken symmetries, inviting the study of  $\rho_s$  to uncover the potentially unconventional nature of its superconductivity. Here we report the measurement of  $\rho_s$  in magic-angle twisted trilayer graphene (TTG), revealing unconventional nodal-gap superconductivity. Utilizing radio-frequency reflectometry techniques to measure the kinetic inductive response of superconducting TTG coupled to a microwave resonator, we find a linear temperature dependence of  $\rho_s$  at low temperatures and nonlinear Meissner effects in the current-bias dependence, both indicating nodal structures in the superconducting order parameter. Furthermore, the doping dependence shows a linear correlation between the zero-temperature  $\rho_s$  and the superconducting transition temperature  $T_c$ , reminiscent of Uemura's relation in cuprates, suggesting phase-coherence-limited superconductivity. Our results provide strong evidence for nodal superconductivity in TTG and put strong constraints on the mechanisms of these graphene-based superconductors.

Superconductivity arises from the condensation of pairs of electrons, known as Cooper pairs, and is characterized by a complex order parameter, comprising an amplitude and a well-defined phase. Microscopically, the amplitude of the order parameter,  $\Delta$ , is related to the strength of Cooper pairing, whereas the superfluid stiffness,  $\rho_s$ , characterizes the phase rigidity of the condensate order parameter. Measurements of  $\rho_s$  are highly motivated not only because phase rigidity is a defining property of the superconducting state, responsible for both zero resistance and the Meissner effect, but also because they help distinguish between conventional and unconventional superconducting orders<sup>1,2</sup>. The dependence of  $\rho_s$  on temperature<sup>1,3</sup> and superfluid velocity<sup>4,5</sup> carries distinctive signatures of the superconducting pairing symmetry. For instance, the linear temperature dependence of  $\rho_s(T)$  in cuprates is the hallmark of nodes in the superconducting order parameter, that is, vanishing  $\Delta$  along a specific direction in momentum space, resulting from the unconventional d-wave pairing in cuprates<sup>6</sup>. The magnitude and doping dependence of  $\rho_s$  also offer deep insights into the details of the superconducting gap and the underlying electron bands<sup>1</sup>.

Notably, in a large class of unconventional superconductors,  $\rho_s$  is orders of magnitude smaller than in conventional Bardeen–Cooper–Schrieffer (BCS)-type superconductors and follows unusual scaling laws<sup>7</sup> relating superconducting phase fluctuations with the superconducting transition temperature ( $T_c$ )<sup>2,8</sup>.

The recent discovery of magic-angle twisted multilayer graphene (MATMG)<sup>9–13</sup> has provided an unprecedented opportunity to study the emergence of superconductivity due to strongly correlated electrons. However, the intense investigations thus far have relied primarily on electrical transport and scanning tunnelling spectroscopy measurements, and the superconducting phase remains poorly understood. Electrical transport experiments varying the displacement field, the magnetic field and the carrier density have shown nematicity<sup>14</sup>, Pauli limit violation<sup>15</sup>, unusual behaviour of the superconducting critical current<sup>16</sup> and correlation with symmetry breaking in the superconducting state<sup>9–11</sup>, suggesting a paradigm beyond BCS physics. However, the zero resistance of the superconducting state precludes any exploration of the internal structure of the superconducting dome using

<sup>1</sup>Department of Physics, Harvard University, Cambridge, MA, USA. <sup>2</sup>Department of Physics, Massachusetts Institute of Technology, Cambridge, MA, USA. <sup>3</sup>Research Center for Electronic and Optical Materials, National Institute for Materials Science, Tsukuba, Japan. <sup>4</sup>Research Center for Materials Nanoarchitectonics, National Institute for Materials Science, Tsukuba, Japan.

<sup>5</sup>Department of Physics, University of Connecticut, Storrs, CT, USA. <sup>6</sup>RTX BBN Technologies, Cambridge, MA, USA. <sup>7</sup>These authors contributed equally: Abhishek Banerjee, Zeyu Hao, Mary Kreidel.

✉e-mail: k.fong@northeastern.edu; pkim@physics.harvard.edu

transport. In contrast, scanning tunnelling spectroscopy studies have shown V-shaped differential conductance spectra, consistent with nodal superconductivity<sup>17,18</sup>. However, this single-particle tunnelling interpretation is complicated by a difficulty in distinguishing superconducting gaps from gaps due to non-superconducting orders such as flavour-polarized correlated states. There is a need to better understand the superconducting order parameter in MATMG calling for measurements of thermodynamic quantities in the superconducting states such as  $\rho_s$ . In particular, measuring  $\rho_s$  allows one to probe inside the superconducting dome, reveal the doping evolution of the superconducting state and provide insights into the origin of superconductivity. However, this has been technically challenging owing to the reduced sample dimensionality and size. Only indirect estimates of  $\rho_s$  based on critical-current density analyses are available so far<sup>16</sup>.

In this work, we use radio-frequency (RF) resonant circuits<sup>19–30</sup> to measure the superfluid response of micrometre-sized twisted trilayer graphene (TTG) superconductors. The microwave response of a superconductor at finite temperatures can be captured by a two-fluid model<sup>31</sup>—a parallel circuit of two channels: the superfluid channel composed of condensed Cooper pairs, and the normal fluid channel composed of quasiparticle excitations. The frequency ( $f$ )-dependent complex RF conductivity in this model can be described by a dissipative real part,  $\sigma_1 = n_n e^2 \tau_n / m_e$  and a dissipationless imaginary part,  $\sigma_2 = n_s e^2 / 2\pi f m_e$ , where  $e$  and  $m_e$  are the electron charge and mass, respectively,  $n_e$  and  $n_s$  are the normal and superfluid electron densities, and  $\tau_n$  is the scattering time for quasiparticle excitations. For the frequency regime  $f < f_c = (n_s / n_n) / 2\pi \tau_n$ ,  $\sigma_1 \ll \sigma_2$ , where  $f_c$  is the cutoff frequency, we expect the impedance of the superconducting sample to be dominated by a dissipationless inductive channel with the characteristic inductance  $L_K = 1 / (2\pi f \sigma_2)$ , often referred to as the kinetic inductance.  $L_K$  is related to the superfluid stiffness by  $\rho_s = (l/w) / (L_K)$  (with units of inverse henry,  $H^{-1}$ ) or  $\rho_s = (l/w) (\hbar^2 / 4e^2 k_B L_K)$  (with units of kelvin, K), where  $w$  and  $l$  are the device width (perpendicular to the current flow) and length, respectively,  $\hbar$  is Planck's constant, and  $k_B$  is Boltzmann's constant. Therefore, by incorporating the superconducting TTG sample into a impedance-matched microwave resonator (Fig. 1a) with a resonance frequency  $f_r$  that shifts linearly with changes of  $L_K$  (see Methods for details), we can measure superfluid stiffness of the TTG sample.

## Superfluid stiffness and nodal superconductivity

Our TTG device consists of three layers of graphene stacked with alternating twist angles of  $\pm\theta = 1.55^\circ$  (ref. 32), encapsulated within a layer of hexagonal boron nitride and graphite on both sides, assembled on an insulating silicon substrate to minimize parasitic capacitance. The graphite layers serve as gate electrodes and can be independently controlled to tune the carrier density and displacement electric field  $D$ . Figure 1b shows an optical microscope image of the device, along with the measurement scheme, where we perform simultaneous d.c. electrical transport and microwave measurements (Methods). Figure 1c shows the four-terminal d.c. resistance  $R$  as a function of filling factor  $\nu$ , defined as the number of carriers per moiré unit cell. We observe superconductivity indicated by zero resistance in the range of filling factors  $-3 < \nu < -2$  for hole doping and  $1.5 < \nu < 3$  for electron doping, with a two-dimensional ( $2D$ )  $\nu$ - $D$  phase diagram (Extended Data Fig. 1b) that is similar to our previous studies<sup>10,11</sup>. Simultaneously, we measure the complex reflection coefficient of the resonator  $S_{21}$ , defined as the ratio between the output (reflected) and input microwave voltage signal  $V_{out}/V_{in}$  (Methods). The amplitude  $|S_{21}|$  as a function of  $\nu$  and frequency  $f$ , as shown in Fig. 1d, shows a dip around 350 MHz due to resonance through the whole range of  $\nu$ , and the resonance shifts to a lower frequency by  $\Delta f_r \approx 10$ –15 MHz as the sample transits from normal to superconducting states. The insets in Fig. 1c show two examples of the  $S_{21}$  amplitude and phase response at the normal and superconducting states, respectively. We use a circle fitting method<sup>33</sup> to accurately

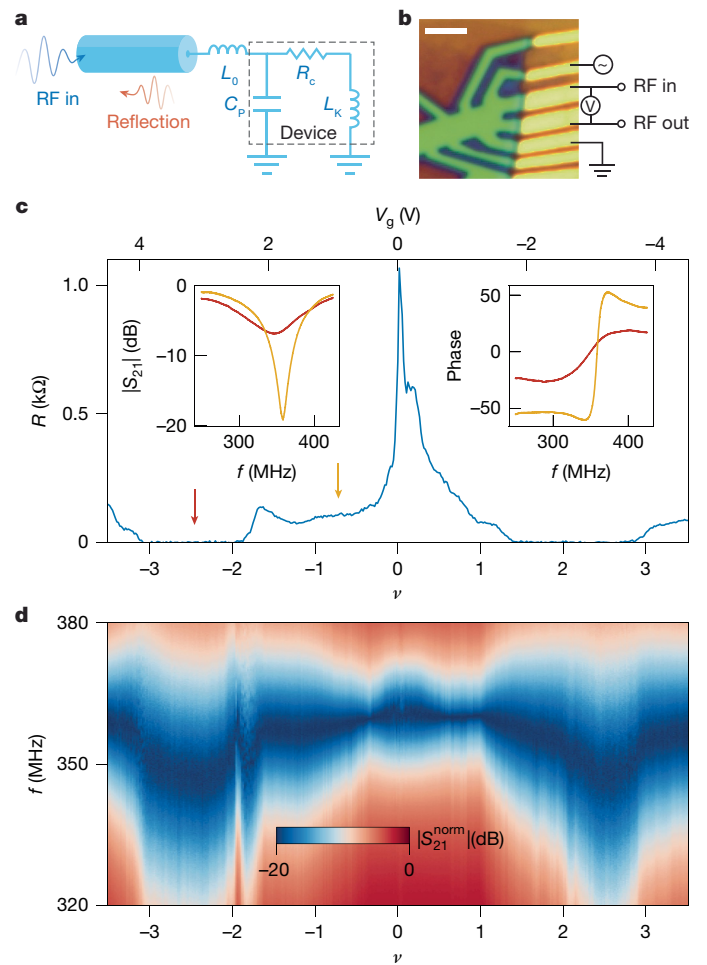


**Fig. 1 | Experimental set-up and device characterization.** **a**, Schematic of the RF reflectometry set-up. An inductor–capacitor (LC) matching network consisting of  $L_0$  (matching inductor) and  $C_p$  (parasitic capacitance) transforms the device impedance 1–10 kΩ to the 50-Ω characteristic impedance of the RF measurement circuit. **b**, Optical microscope image of the TTG device reported in the main text and a simple schematic of the measurement scheme. Scale bar, 3 μm. **c**, The d.c. resistance  $R$  of the device as a function of moiré filling factor  $\nu$ . The sample is superconducting ( $R = 0$ ) in both the electron- and hole-doped sectors. Insets: the amplitude and phase response of the complex reflection coefficient  $S_{21}$  showing shifts in resonance frequency between the normal and superconducting states. **d**, Two-dimensional map of the normalized amplitude  $|S_{21}^{norm}|$  shown as a function of frequency  $f$  and filling factor  $\nu$ . For clearer visualization, for each  $\nu$ , we define its  $|S_{21}^{norm}(f)| = 1 - (\max(|S_{21}(f)|) - |S_{21}(f)|) / 0.9$ . The resonator undergoes large frequency shifts  $\Delta f_r \approx 10$ –15 MHz when the sample changes from normal to superconducting states.

extract the resonance frequency  $f_r$ , from which we estimate  $L_K$  and  $\rho_s = (l/w) (\hbar^2 / 4e^2 L_K)$ . In this analysis, we used  $l/w \approx 5$  based on the device geometry (Methods).

Focusing on the hole-side superconductor, we measure  $R$  and  $f_r$  as a function of  $\nu$  and temperature  $T$ .  $R(\nu, T)$  shows a superconducting dome manifesting as the zero-resistance area in Fig. 2a, with a maximum  $T_c = 1.2$  K at the optimal doping  $\nu_{op} = -2.3$ , where  $T_c$  is defined as the temperature at which the device resistance is 5% of the normal-state resistance. Correspondingly,  $f_r(\nu, T)$  in Fig. 2b also shows a dome of lower resonance frequency in about the same area. Converting  $f_r$  to  $\rho_s$ , in Fig. 2c we plot the temperature dependence of  $\rho_s$  in the units of both inverse nanohenry and kelvin at several filling factors around  $\nu_{op}$  within the superconducting dome. Across these filling factors,  $\rho_s(T)$  increases linearly with decreasing  $T$ , with no sign of saturation down to the lowest measurable temperature, about 30 mK.

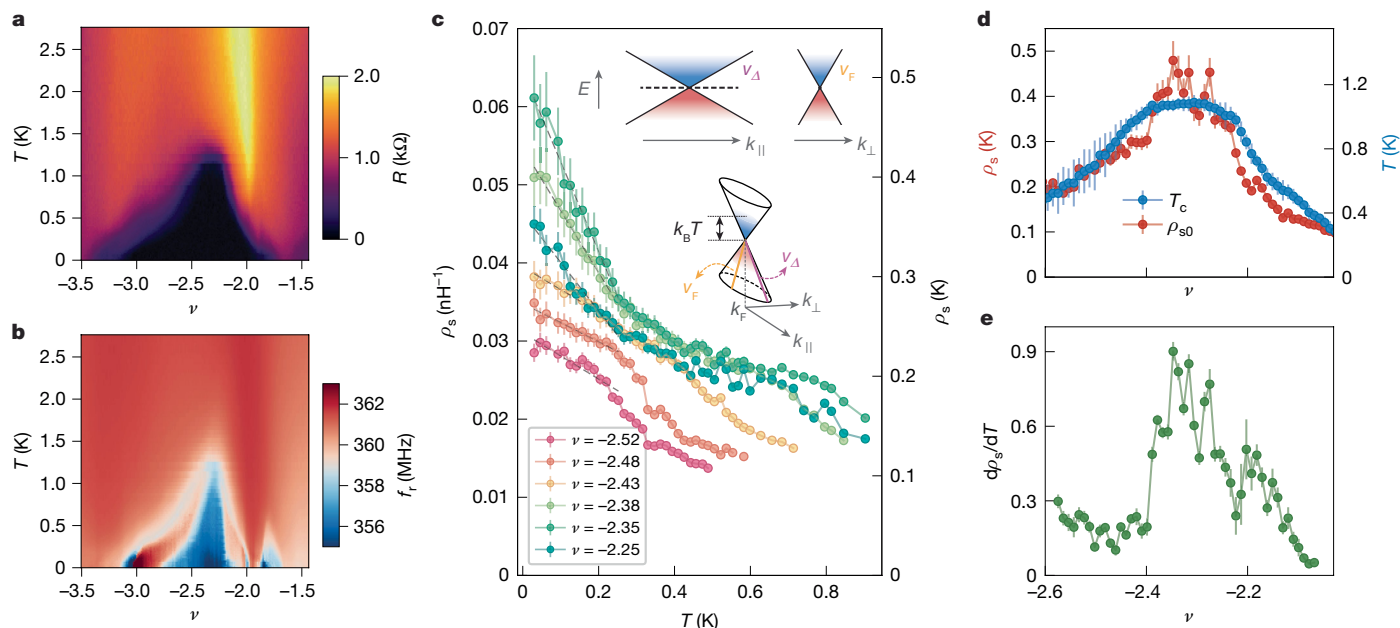


**Fig. 2 | Temperature- and doping-dependent superfluid stiffness.** **a, b**, Two-dimensional map of the d.c. resistance  $R$  (**a**) and the resonator frequency  $f_r$  (**b**) measured as a function of moiré filling factor  $\nu$  and sample temperature  $T$ . **c**, Superfluid stiffness  $\rho_s$  as a function of  $T$  for a range of filling factors around  $\nu = -2.4$ . Inset: the low-energy dispersion of quasiparticles near gap nodes. The top two schematics depict the dispersion along  $k_{||}$  and  $k_{\perp}$ , the lattice momentum parallel and perpendicular to the electron Fermi surface, respectively. Their slopes are characterized by two distinct velocities:  $v_{\Delta}$  and

the Fermi velocity  $v_F$ , resulting in the anisotropic cone dispersion shown in the schematic below. The dashed line denotes the Fermi energy. The blue and red colours represent excited quasiparticles and quasiholes, respectively, with energies of order  $\pm k_B T$  from the Fermi energy.  $k_F$  represents the Fermi momentum where the node resides. **d**, Left axis: zero-temperature superfluid stiffness obtained by linear extrapolation of curves in **c**, as a function of  $\nu$ . Right axis:  $T_c$  obtained from d.c. resistance measurements as a function of  $\nu$ . **e**, Low-temperature slope  $d\rho_s/dT$  obtained as a function of  $\nu$ .

This linear-in- $T$  behaviour is consistent with a 2D nodal superconducting order, where the superconducting gap vanishes along certain directions—referred to as ‘nodes’—on the Fermi surface<sup>1,3</sup>. Nodal points lead to a gapless linear dispersion for quasiparticle excitations characterized by two distinct velocities:  $v_{\Delta}$  and  $v_F$ , representing the slope of the superconducting gap and the Fermi velocity, respectively (Methods and Fig. 2c, inset). A non-zero  $T$  would immediately populate this gapless cone with equal numbers of quasiparticles and quasiholes, resulting in a linear-in- $T$  suppression of  $\rho_s(T)$ . Our measurements indicate that the superconducting gap is nodal across the entire superconducting dome. We emphasize that this linear-in- $T$  behaviour occurs below  $T \approx 0.2$ – $0.5$  K  $\approx T_c/2$  and covers approximately an order of magnitude in temperature. We contrast this with the saturating  $\rho_s(T)$  observed in our stiffness measurements of niobium nitride (NbN) thin films (Extended Data Fig. 5).

### BKT transition and Uemura’s law

We further characterize the doping dependence of the low-temperature linear behaviour of  $\rho_s$  by performing a linear fit, as indicated by the dashed lines in Fig. 2c. From this fit, we extract the zero-temperature limit of the superfluid stiffness  $\rho_{s0} = \rho_s(T = 0)$  and the slope  $d\rho_s/dT$ , shown in Fig. 2d,e, respectively. In Fig. 2d, we compare  $\rho_{s0}$  with  $T_c$  extracted from d.c. measurements. The two quantities roughly track each other in a bell-shaped curve centred around  $\nu = -2.3$ , suggesting that the same mechanism determines both  $\rho_{s0}(\nu)$  and  $T_c(\nu)$ . In contrast, the low-temperature slope  $d\rho_s/dT$  is roughly constant, about 0.2–0.3 for  $-2.6 < \nu < -2.4$ , and then shows a sharp change rising to nearly about 0.9 around  $\nu = -2.3$  before tapering off to about 0 as we approach the right edge of the dome at  $\nu = -2$ .

Considering that TTG superconductivity is a strictly 2D phenomenon, the experimentally obtained  $\rho_s(T)$  allows us to estimate the Berezinskii–Kosterlitz–Thouless (BKT) transition temperature  $T_0$  using the Nelson–Kosterlitz criterion:  $T_{\text{BKT}} = \pi \rho_s(T_{\text{BKT}})/2$  (ref. 34), by locating the

temperature  $T_0$  where  $\rho_s(T, \nu)$  (smoothed for clarity) intersects with the universal critical stiffness  $\rho_c = 2T/\pi$  plane (Fig. 3a). As shown in the top panel of Fig. 3a and indicated by the ratio between the slopes of  $T_c(\rho_{s0})$  and  $T_0(\rho_{s0})$  in Fig. 3b, we find  $T_c/T_0 \approx 3.0$ , where  $T_c$  is obtained from the d.c. transport. We ascribe this factor to sample inhomogeneity<sup>35,36</sup> (Methods) that results in a network of percolating superconducting paths with an effective width  $w^* < w$  (Fig. 3b, inset). Considering  $T_{\text{BKT}} \approx T_c$  in MATMG<sup>10,11</sup> (that is, zero resistivity for  $T < T_{\text{BKT}}$ ), we can estimate an effective aspect-ratio parameter  $\alpha = w/w^* \approx T_{\text{BKT}}/T_0 \approx T_c/T_0 \approx 3.0$ . Therefore,  $\rho_s$  obtained from the measured kinetic response underestimates the true superfluid stiffness by a factor of  $\alpha$  (see Methods for details).

Having obtained  $\alpha$ , we make quantitative comparison between  $\rho_{s0}$  and  $T_c$  (Fig. 3b). We find a linear correlation between  $\rho_{s0}$  and  $T_c$  away from the optimal doping—in both underdoped ( $\nu > \nu_{\text{op}}$ ) and overdoped ( $\nu < \nu_{\text{op}}$ ) regimes. A linear dependence of  $T_c$  on  $\rho_{s0}$  was first identified in underdoped cuprates<sup>7</sup>, and subsequently observed in a variety of unconventional superconductors including overdoped cuprates<sup>37–39</sup>, suggesting a universal scaling behaviour known as the Uemura’s relation. This phenomenological dependence suggests that long-range phase order, characterized by  $\rho_{s0}$ , determines  $T_c$ , in contrast to conventional BCS superconductors where the strength of Cooper pairing, characterized by the BCS gap  $\Delta$ , determines  $T_c$ . Following this interpretation and taking into account the non-parabolic band dispersion in TTG shown in Fig. 3c discussed below, we estimate  $T_c/E_F \approx 0.03$ – $0.08$  (Methods), where  $E_F$  is the Fermi energy. This result indicates strongly coupled superconductivity, consistent with more indirect analyses in previous studies<sup>10,11</sup>. Furthermore, the coupling strength becomes weaker on the overdoped side, similar to cuprate superconductors.

### Electron–electron interactions in flat bands

We now focus on the density-dependent behaviours of  $\rho_{s0}$  and  $d\rho_s/dT$  measured at the zero-temperature limit. Recalling that  $\rho_s = \hbar^2 n_s / (4m_e)$



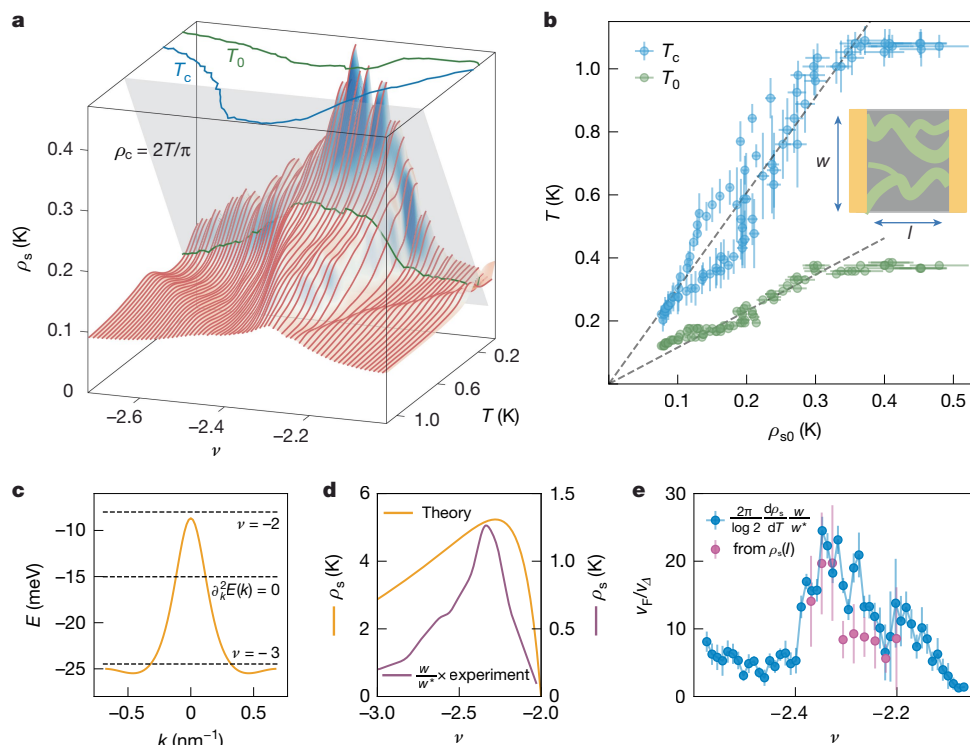


**Fig. 3 | BKT transition, Uemura's relation and nodal pairing symmetry.**

**a**, Waterfall plot showing  $\rho_s$  as a function of  $T$  and  $\nu$ . To aid visualization, the curves have been interpolated and smoothed with a six-point moving average along the  $T$  axis. The BKT transition temperature ( $T_0$ ) is obtained from the intersection between the universal BKT plane represented as  $\rho_c = 2T/\pi$  and the experimental stiffness curves. **b**,  $T_c$  and  $T_0$  plotted against  $\rho_{s0}$ . Inset: schematic showing inhomogeneous superconducting paths that may lead to an underestimation of the superfluid stiffness. **c**, Hartree-Fock renormalized bands in TTG as a function of momentum  $k$  within the mini-Brillouin zone.

The dashed lines mark the energy where  $\nu = -2$ ,  $\nu = -3$  and the curvature  $\partial_k^2 E(k) = 0$  occur. **d**, Comparison of the theoretical estimation of  $\rho_{s0}(\nu)$  based on the Hartree-Fock renormalized band structure, with the experimentally obtained  $\rho_{s0}(\nu)$ , which is also interpolated and smoothed for clarity. Both theory and experiment show a bell-shaped  $\nu$  dependence, with a lopsided maximum close to  $\nu = -2$ . Theory estimates are larger by five times compared with the experimental value. **e**,  $\nu_F/\nu_\Delta$  as a function of  $\nu$  obtained from the temperature dependence  $\rho_s(T)$  and the current-bias dependence  $\rho_s(I)$  (described later). The two methods roughly agree with  $\nu_F/\nu_\Delta \approx 2-20$ .

for parabolic bands described by an effective mass  $m_e$ , we expect a linear relationship between  $\rho_{s0}$  and  $\nu \propto n_s$ . The bell-shaped dependence observed in the experiment (Fig. 2d), particularly the drop of  $\rho_{s0}$  with increasing hole doping for  $\nu < -2.4$ , suggests a departure from the parabolic band approximation. Theoretical modelling of the TTG band structure for moiré fillings between  $-3 < \nu < -2$  suggests the presence of strongly renormalized band dispersion  $E(k)$  that is highly non-parabolic, where  $E$  is the energy and  $k$  is the lattice momentum magnitude, as shown in Fig. 3c, obtained by Hartree-Fock calculation assuming flavour polarization of the TTG flat band. An interplay between strong Coulomb repulsion and quantum geometric effects, particularly the concentration of Berry curvature near  $k = 0$ , leads to a band structure that is highly dispersive close to  $\nu = -2$  but becomes progressively flatter on approaching  $\nu = -3$ . For such non-parabolic bands, a more general formula is required for the superfluid stiffness:  $\rho_s(\nu) = \frac{1}{8} \sum_{\mathbf{k}} n_{\mathbf{k}} \nabla_{\mathbf{k}}^2 E = \frac{\nu_F(\nu) k_F(\nu)}{8\pi}$  (for an isotropic  $E(\mathbf{k})$ ), where  $k_F$  is the Fermi momentum, leading to a doping dependence as shown in the theoretical estimate in Fig. 3d (in yellow). This agrees qualitatively with the smoothed experimental curve shown in red.

With the geometrical correction  $\alpha$  included, we also provide a quantitative analysis on the low-temperature linear dependence of  $\rho_s(T)$ . Within the physical picture of nodal superconducting gaps, the aforementioned gap and electron band velocities  $v_\Delta$  and  $v_F$  are related to the linear slope of  $\rho_s(T)$  by  $\nu_F/\nu_\Delta = (8\pi/N \log(2)) d\rho_s/dT \times \alpha$ , where  $N$  is the number of nodes (see Methods for details). Tentatively assuming  $N = 4$  (d wave) and considering the scaling factor  $\alpha = 3$ , we obtain  $\nu_F/\nu_\Delta \approx 5-20$  as a function of  $\nu$ , as shown in Fig. 3e. We also estimate  $\nu_F/\nu_\Delta$  from current-bias dependent measurements  $\rho_s(I)$  (discussed below),

and obtain similar values (Fig. 3e), suggesting the robustness of our estimation of  $\nu_F/\nu_\Delta$ .

## Nonlinear Meissner effect

We also investigate the behaviour of  $\rho_s$  in the presence of a finite d.c. supercurrent bias  $I$ . Within the superconducting regime indicated by the dark regions of zero resistance  $R(I, T)$  in Fig. 4a and  $R(\nu, T)$  in Fig. 4b, we measure a rapid suppression of  $\rho_s$  with increasing  $I$  (Fig. 4c,d), with the strongest signatures close to a range of filling factors around the optimal doping ( $\nu = -2.3$ , where the critical current  $I_c \approx 0.12 \mu\text{A}$ ; Fig. 4d). The suppression of  $\rho_s$ ,  $\delta\rho_s$ , follows a quadratic behaviour with a quadratic coefficient  $b$ ,  $\delta\rho_s = -bI^2$ , close to  $I \rightarrow 0$ , which turns linear with a linear coefficient  $c$ ,  $\delta\rho_s = -cI$ , after  $I$  exceeds a crossover current scale  $I^*$ . Close to the optimal doping ( $\nu = -2.34$ ), we find that the quadratic behaviour at low bias is strongly temperature dependent (Fig. 4c) with the quadratic coefficient  $b$  appearing to diverge as  $T \rightarrow 0$  (Fig. 4e). We also observe a non-trivial filling factor dependence of both the quadratic coefficient,  $b(\nu)$ , and the linear coefficient,  $c(\nu)$ , measured at  $T = 30 \text{ mK}$  (Fig. 4f,g).

These observations are consistent with the nonlinear Meissner effect of 2D nodal superconductors<sup>4,40-42</sup>, where a supercurrent  $I$  produces a Doppler shift of the quasiparticle spectrum owing to finite superfluid velocity, resulting in a current-dependent quasiparticle population at the nodal points. Our model (Methods) quantitatively captures all experimental features and allows independent estimation of  $\nu_F$  and  $\nu_\Delta$  (Fig. 4h). In particular, the divergence of  $b(T \rightarrow 0)$  is a strong signature of nodal superconductivity that cannot be easily mimicked by anisotropically gapped superconducting states, providing an additional

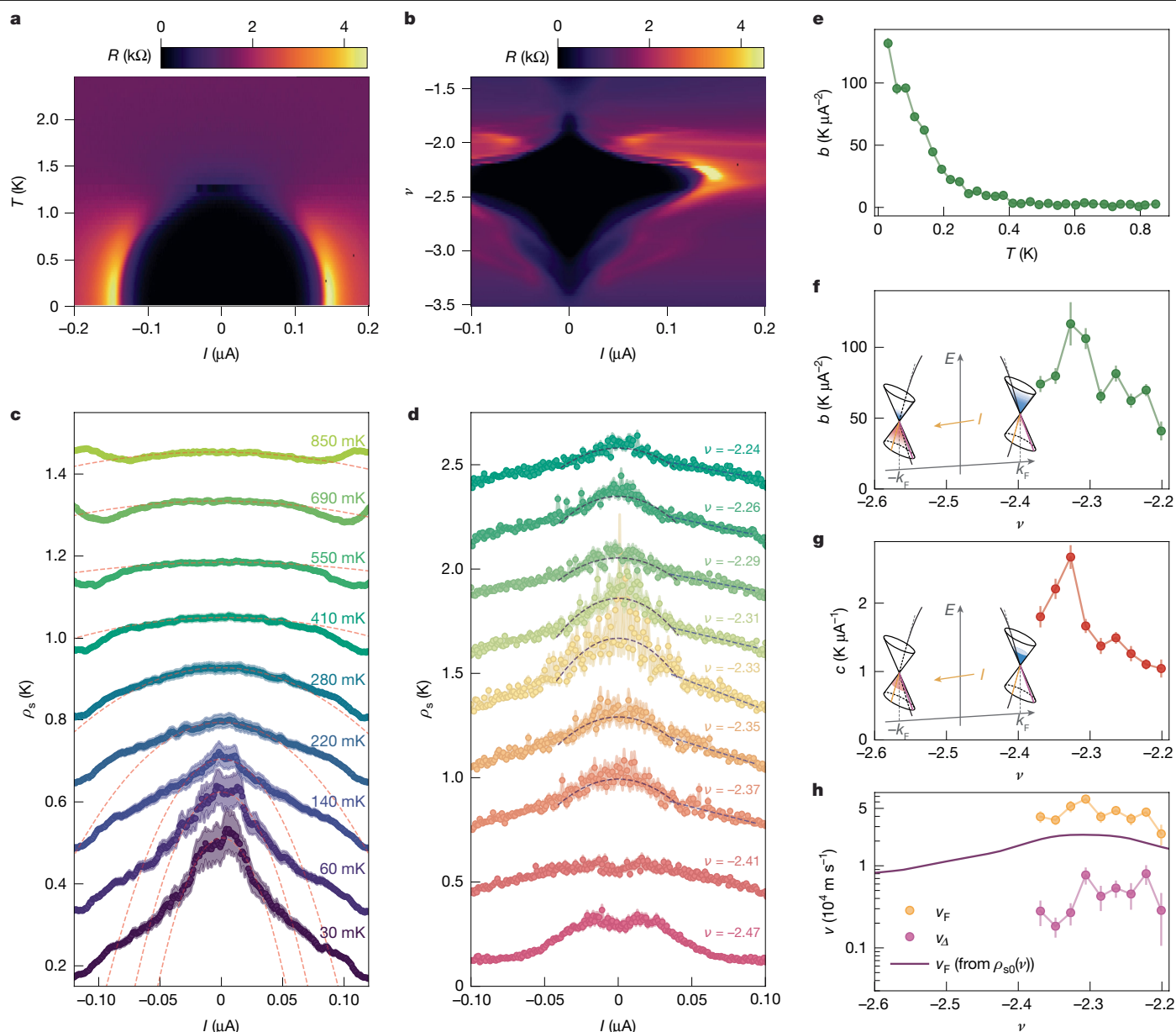


**Fig. 4 | Nonlinear Meissner effect.** **a**, Two-dimensional map of the d.c. resistance  $R$  as a function of current bias  $I$  and temperature  $T$  close to optimal doping  $\nu = -2.34$  where critical current  $I_c \approx 0.12 \mu\text{A}$  is maximum. **b**,  $R$  as a function of supercurrent bias  $I$  and moiré filling factor  $\nu$ . **c**,  $\rho_s(I)$  measured at  $\nu = -2.34$  at different values of sample temperature  $T$ . The curvature of  $\rho_s(I)$  at zero current decays with increasing temperature. **d**, Superfluid stiffness  $\rho_s$  as a function of  $I$  for a range of filling factors  $\nu = -2.24$  to  $\nu = -2.47$  ( $T = 30 \text{ mK}$ ). For a range of filling factors around optimal doping,  $\rho_s(I) \propto -I^2$  for  $I \rightarrow 0$  with a crossover to linear dependence  $\rho_s(I) \propto -I$ . The linear behaviour persists for a large range of  $I < I_c \approx 0.12 \mu\text{A}$  around  $\nu = -2.34$ . Curves are shifted for clarity. **e**, Temperature dependence of the curvature of  $\rho_s(I)$  at  $I = 0$ ,  $b(T)$ . Diverging behaviour is observed as  $T \rightarrow 0$ ,

a strong signature of nodal superconductivity. **f, g**, Base temperature value of the quadratic curvature  $b$  (**f**) and the linear slope  $c$  (**g**) as a function of moiré filling factor. **h**, Fermi velocity estimated from  $\rho_s(I)$  and  $\rho_s(T)$ , indicating  $v_F \approx 0.1 \times 10^5$ – $0.7 \times 10^5 \text{ m s}^{-1}$  and  $v_A \approx 0.2 \times 10^4$ – $0.5 \times 10^4 \text{ m s}^{-1}$ . The solid line shows  $v_F$  calculated using the interpolated and smoothed experimental  $\rho_{s0}(\nu)$ . Insets: schematics depicting the two different regimes of the nonlinear Meissner effect. In **f**,  $I > 0$ , both temperature and current produce quasiparticle excitations. In **g**,  $I > I^*$ , the current-induced effect dominates over temperature. In both cases, the current bias produces a finite population of quasiparticles in one node and quasiholes in the opposite node.

signature of nodal pairing symmetry<sup>42–44</sup>. Similar divergences of  $b(T)$  are measured in a second device at optimal doping of both the electron-like and hole-like superconducting sectors (Supplementary Fig. 6).

## Summary

Our superfluid stiffness measurements provide insights into the nature of superconductivity in MATMG. A confluence of signatures, including the linear-in- $T$  suppression of superfluid stiffness, the observation of the nonlinear Meissner effect, and its temperature dependence,

provides strong evidence for a nodal pairing symmetry. The linear scaling relation between superfluid stiffness at the zero-temperature limit and the superconducting transition temperature suggests an unusual scenario where the superconducting transition is controlled by phase fluctuations rather than Cooper-pair breaking.

## Online content

Any methods, additional references, Nature Portfolio reporting summaries, source data, extended data, supplementary information,

acknowledgements, peer review information; details of author contributions and competing interests; and statements of data and code availability are available at <https://doi.org/10.1038/s41586-024-08444-3>.

- Lee, P. A. & Wen, X.-G. Unusual superconducting state of underdoped cuprates. *Phys. Rev. Lett.* **78**, 4111 (1997).
- Emery, V. J. & Kivelson, S. A. Importance of phase fluctuations in superconductors with small superfluid density. *Nature* **374**, 434–437 (1995).
- Millis, A. J., Girvin, S. M., Ioffe, L. B. & Larkin, A. I. Anomalous charge dynamics in the superconducting state of underdoped cuprates. *J. Phys. Chem. Solids* **59**, 1742–1744 (1998).
- Yip, S. K. & Sauls, J. A. Nonlinear Meissner effect in CuO superconductors. *Phys. Rev. Lett.* **69**, 2264 (1992).
- Xu, D., Yip, S. K. & Sauls, J. A. Nonlinear Meissner effect in unconventional superconductors. *Phys. Rev. B* **51**, 16233 (1995).
- Hardy, W. N., Bonn, D. A., Morgan, D. C., Liang, R. & Zhang, K. Precision measurements of the temperature dependence of  $\lambda$  in YBCO: strong evidence for nodes in the gap function. *Phys. Rev. Lett.* **70**, 3999 (1993).
- Uemura, Y. J. et al. Universal correlations between  $T_c$  and  $n/m^*$  (carrier density over effective mass) in high- $T_c$  cuprate superconductors. *Phys. Rev. Lett.* **62**, 2317 (1989).
- Keimer, B., Kivelson, S. A., Norman, M. R., Uchida, S. & Zaanen, J. From quantum matter to high-temperature superconductivity in copper oxides. *Nature* **518**, 179–186 (2015).
- Cao, Y. et al. Unconventional superconductivity in magic-angle graphene superlattices. *Nature* **556**, 43–50 (2018).
- Hao, Z. et al. Electric field-tunable superconductivity in alternating-twist magic-angle trilayer graphene. *Science* **371**, 1133–1138 (2021).
- Park, J. M., Cao, Y., Watanabe, K., Taniguchi, T. & Jarillo-Herrero, P. Tunable strongly coupled superconductivity in magic-angle twisted trilayer graphene. *Nature* **590**, 249–255 (2021).
- Park, J. M. et al. Robust superconductivity in magic-angle multilayer graphene family. *Nat. Mater.* **21**, 877–883 (2022).
- Zhang, Y. et al. Promotion of superconductivity in magic-angle graphene multilayers. *Science* **377**, 1538–1543 (2022).
- Cao, Y. et al. Nematicity and competing orders in superconducting magic-angle graphene. *Science* **372**, 264–271 (2021).
- Cao, Y., Park, J. M., Watanabe, K., Taniguchi, T. & Jarillo-Herrero, P. Pauli-limit violation and re-entrant superconductivity in moiré graphene. *Nature* **595**, 526–531 (2021).
- Tian, H. et al. Evidence for Dirac flat band superconductivity enabled by quantum geometry. *Nature* **614**, 440–444 (2023).
- Oh, M. et al. Evidence for unconventional superconductivity in twisted bilayer graphene. *Nature* **600**, 240–245 (2021).
- Kim, H. et al. Evidence for unconventional superconductivity in twisted trilayer graphene. *Nature* **606**, 494–500 (2022).
- Schoelkopf, R. J., Wahlgren, P., Kozhevnikov, A. A., Delsing, P. & Prober, D. E. The radio-frequency single-electron transistor (RF-SET): a fast and ultrasensitive electrometer. *Science* **280**, 1238–1242 (1998).
- Reilly, D. J., Marcus, C. M., Hanson, M. P. & Gossard, A. C. Fast single-charge sensing with a RF quantum point contact. *Appl. Phys. Lett.* **91**, 162101 (2007).
- Vigneau, F. et al. Probing quantum devices with radio-frequency reflectometry. *Appl. Phys. Rev.* **10**, 021305 (2023).
- Crossno, J. et al. Observation of the Dirac fluid and the breakdown of the Wiedemann–Franz law in graphene. *Science* **351**, 1058–1061 (2016).
- Annuziata, A. J. et al. Tunable superconducting nanoinductors. *Nanotechnology* **21**, 445202 (2010).
- Singh, G. et al. Competition between electron pairing and phase coherence in superconducting interfaces. *Nat. Commun.* **9**, 407 (2018).
- Weitzel, A. et al. Sharpness of the Berezinskii–Kosterlitz–Thouless transition in disordered NbN films. *Phys. Rev. Lett.* **131**, 186002 (2023).
- Haller, R. et al. Phase-dependent microwave response of a graphene Josephson junction. *Phys. Rev. Res.* **4**, 013198 (2022).
- Phan, D. et al. Detecting induced  $p \pm ip$  pairing at the Al–InAs interface with a quantum microwave circuit. *Phys. Rev. Lett.* **128**, 107701 (2022).
- Böttcher, C. G. L. et al. Circuit quantum electrodynamics detection of induced two-fold anisotropic pairing in a hybrid superconductor–ferromagnet bilayer. *Nat. Phys.* **20**, 1609–1615 (2024).
- Tanaka, M. et al. Superfluid stiffness of magic-angle twisted bilayer graphene. *Nature* <https://doi.org/10.1038/s41586-024-08494-7> (2025).
- Kreidel, M. et al. Measuring kinetic inductance and superfluid stiffness of two-dimensional superconductors using high-quality transmission-line resonators. Preprint at <https://arxiv.org/abs/2407.09916> (2024).
- Tinkham, M. *Introduction to Superconductivity* 2nd edn (Dover Publications, 2004).
- Khalaf, E., Kruchkov, A. J., Tarnopolsky, G. & Vishwanath, A. Magic angle hierarchy in twisted graphene multilayers. *Phys. Rev. B* **100**, 085109 (2019).
- Probst, S., Song, F. B., Bushev, P. A., Ustinov, A. V. & Weides, M. Efficient and robust analysis of complex scattering data under noise in microwave resonators. *Rev. Sci. Instrum.* **86**, 024706 (2015).
- Nelson, D. R. & Kosterlitz, J. M. Universal jump in the superfluid density of two-dimensional superfluids. *Phys. Rev. Lett.* **39**, 1201 (1977).
- Turkel, S. et al. Orderly disorder in magic-angle twisted trilayer graphene. *Science* **376**, 193–199 (2022).
- Uri, A. et al. Mapping the twist-angle disorder and Landau levels in magic-angle graphene. *Nature* **581**, 47–52 (2020).
- Homes, C. C. et al. A universal scaling relation in high-temperature superconductors. *Nature* **430**, 539–541 (2004).
- Dordevic, S. V., Basov, D. N. & Homes, C. C. Do organic and other exotic superconductors fail universal scaling relations? *Sci. Rep.* **3**, 1713 (2013).
- Božović, I., He, X., Wu, J. & Bollinger, A. T. Dependence of the critical temperature in overdoped copper oxides on superfluid density. *Nature* **536**, 309–311 (2016).
- Bidinosti, C. P., Hardy, W. N., Bonn, D. A. & Liang, R. Magnetic field dependence of  $\lambda$  in YBa<sub>2</sub>Cu<sub>3</sub>O<sub>6.95</sub>: results as a function of temperature and field orientation. *Phys. Rev. Lett.* **83**, 3277–3280 (1999).
- Oates, D. E., Park, S.-H. & Koren, G. Observation of the nonlinear Meissner effect in YBCO thin films: evidence for a d-wave order parameter in the bulk of the cuprate superconductors. *Phys. Rev. Lett.* **93**, 197001 (2004).
- Wilcox, J. A. et al. Observation of the non-linear Meissner effect. *Nat. Commun.* **13**, 1201 (2022).
- Dahm, T. & Scalapino, D. J. Theory of microwave intermodulation in a high- $T_c$  superconducting microstrip resonator. *Appl. Phys. Lett.* **69**, 4248–4250 (1996).
- Bae, S. et al. Dielectric resonator method for determining gap symmetry of superconductors through anisotropic nonlinear Meissner effect. *Rev. Sci. Instrum.* **90**, 043901 (2019).

**Publisher's note** Springer Nature remains neutral with regard to jurisdictional claims in published maps and institutional affiliations.

Springer Nature or its licensor (e.g. a society or other partner) holds exclusive rights to this article under a publishing agreement with the author(s) or other rightsholder(s); author self-archiving of the accepted manuscript version of this article is solely governed by the terms of such publishing agreement and applicable law.

© The Author(s), under exclusive licence to Springer Nature Limited 2025

## Methods

### Device fabrication

We prepared the TTG heterostructures using the standard dry-transfer method, where we used stamps consisting of polycarbonate polymer and polydimethylsiloxane to pick up each 2D material flake sequentially. The TTG heterostructures consisted of hexagonal boron nitride (hBN)/graphite/hBN/TTG/hBN/graphite/hBN, from top to bottom. Graphite flakes were used as top and bottom gates to control the density and displacement field in TTG. The three pieces of TTG came from the same monolayer graphene, which was pre-cut into three with a laser.

To make the TTG structure, we picked up each piece sequentially, with a rotation angle  $\theta$  and  $-\theta$  applied to the stage before picking the second and third piece, respectively. After picking up all layers, we dropped the stack onto an undoped silicon substrate, which created a much lower parasitic capacitance than a doped silicon substrate in the RF measurements. We then etched the stack into a Hall bar geometry and deposited chromium/gold contacts through standard nanofabrication lithography. We intentionally made the contacts wide, especially for those used for RF measurements, given that RF reflectometry is intrinsically a two-terminal measurement and benefits from a wide, uniform sample path. We also minimized the area between the gold–TTG edge contact region and the double-gated TTG channel region so that the two-terminal signal was dominated by the channel region, in addition to the inevitable contact resistance.

### Measurements

Measurements were performed in a Bluefors dilution refrigerator with a base electron temperature of  $T = 20$  mK, achieved with extensive filtering, shielding and thermal coupling of the sample within copper packaging. The d.c. transport measurements were performed using the a.c. lock-in technique with an excitation current of 1–10 nA and a low excitation frequency of about 17 Hz. All d.c. lines were filtered using a set of resistor–capacitor filters mounted on a 4-K plate and inductor–capacitor filters, to avoid dissipation, mounted at the mixing chamber. The device was embedded in the resonant circuit by way of bias tees and wire bonding the reflectometry line to one of the sample leads, and another lead provided the RF ground. Reflectometry measurements were performed using a vector network analyser (VNA). The RF excitation signal generated from the VNA was first attenuated by 32 dB by cryostat attenuators installed at various stages of the fridge, and then by another 20 dB as it passed from the coupled port to the in-port of the directional coupler installed below the mixing chamber. The directional coupler provided a means to remove any spurious resonances in the background of the measurement chain by subtracting the sample signal from the measured gain line without the sample. This allowed us to precisely quantify the sample resonance shift, and subsequently its superfluid stiffness, without contributions from the measurement chain. After reflection from the resistor–inductor–capacitor circuit, the signal passes through a K&L filter (450 MHz cut-off), is amplified by 40 dB using a cryogenic amplifier (Weinreb CITLF3) mounted on the 4-K plate, and amplified again by 40 dB using a room-temperature amplifier before being measured by the VNA (Extended Data Fig. 2). The RF power incident on the sample was varied from  $-112$  dBm to  $-102$  dBm. Measurements were performed with a bandwidth of 0.5–1 kHz, with each VNA trace averaged 5–10 times. We measured the superfluid stiffness of fabricated NbN thin film wires in series with resistors similar to the contact resistance of our TTG devices to ensure that our high-frequency set-up did not produce temperature-dependent artefacts (Extended Data Fig. 5).

### Sample thermalization

We wait for 15–20 minutes at each value of the mixing chamber temperature for the sample temperature to equilibrate. To avoid sample thermalization issues, we combined a number of techniques: extensive

filtering, judicious cryostat wiring and shielding. All d.c. lines were filtered using a set of resistor–capacitor (RC) filters mounted on the 4-K plate and inductor–capacitor (LC) filters mounted at the mixing chamber. The efficient thermalization of the sample is evident in our measurements, as the stiffness data change even at the lowest temperatures (25 mK) for every temperature setpoint (Fig. 2c). In particular, as shown in Fig. 4e, we observe that  $b(T)$  shows a  $1/T$  behaviour down to lowest temperatures. However, a constant temperature offset between the sample and the mixing chamber cannot be ruled out. Such an offset would not affect our main conclusions concerning the linear-in- $T$  dependence of superfluid stiffness. Furthermore, residual quasiparticles of non-thermal origin, as observed in aluminium<sup>45</sup>, may lead to a constant temperature-independent shift of the resonator frequency; however, the qualitative behaviour of  $\rho_s(T)$  is expected to remain unchanged. Superfluid stiffness measurements of aluminium in the same dilution fridge showed BCS-like saturation of  $\rho_s(T)$ , providing additional evidence for efficient thermalization<sup>30</sup>.

### RF resonator method

Techniques utilizing RF resonators have been used to measure kinetic inductances<sup>23–26</sup>, including the recent use of superconducting resonant circuits for the detection of intraband pairing in superconductor–semiconductor hybrids<sup>27</sup> and twofold anisotropic pairing in superconductor–ferromagnet hybrids<sup>28</sup>. However, integrating superconducting resonators with 2D material flakes remains difficult, with encouraging recent progress<sup>29,30</sup>. In addition, the large inherent contact resistance  $R_c \approx 1$ –10 k $\Omega$  and parasitic capacitive coupling  $C_p$  in 2D material devices (Fig. 1a) can completely damp out resonances, making measurements of  $L_K$  in 2D van der Waals superconductors challenging. We solve this problem by using an impedance-matching network and adding a surface-mount inductor  $L_0$ . Under our experimental conditions,  $C_p \approx 1$ –10 pF and a choice of  $L_0 \approx 100$ –200 nH allows the combined impedance of the resonant circuit,  $Z_D \approx L_0/(C_p R_c)$ , to match the characteristic RF matching impedance  $Z_0 = 50 \Omega$ , resulting in lumped-element microwave resonant circuits with a resonance frequency  $f_{r0} = 1/2\pi\sqrt{L_0 C_p} \approx 100$ –300 MHz. Changes in the kinetic inductance produce relative shifts of the microwave resonance frequency  $\Delta f_r/f_{r0}$ , and they are related by a linear relationship  $\Delta L_K = 2R_c^2 C_p (\Delta f_r/f_{r0})$  for expected values of  $L_K \approx 10$ –100s of nanohenrys  $\leq 0.1 R_c^2 C_p \approx 1 \mu\text{H}$  (Methods). We contrast our approach with other experimental methods to measure superfluid stiffness that do not readily integrate with 2D material flakes<sup>23,24</sup>, have high operating frequencies<sup>27</sup> or require macroscopic-sized samples<sup>39</sup>.

Supplementary Fig. 1a shows a schematic of the effective microwave resonant circuit, where  $L_0$  is the externally added inductor,  $C_p$  represents the parasitic capacitance arising primarily from the circuit board, bond wires and the substrate, but may also be added externally in parallel,  $R_c$  is the contact resistance and  $L_K$  is the inductance of the device in the superconducting state. This circuit can be simplified to an effective series resistor–inductor–capacitor model, shown in Supplementary Fig. 1b where, using the method of series–parallel transformations, we obtain  $R_{\text{eff}} = L_0/(R_c C_{\text{eff}})$  and  $C_{\text{eff}} = (C_p - L_0/R_c^2 + L_K/R_c^2)$ , where  $R_{\text{eff}}$  is the effective resistance and  $C_{\text{eff}}$  is the effective capacitance. Modelling the resonator as a series resistor–inductor–capacitor circuit coupled to a  $Z_0 = 50 \Omega$  transmission line, we can express the impedance of the resonator as:

$$Z = R_{\text{eff}} + 2\pi i f L_0 + \frac{1}{2\pi i f C_{\text{eff}}} \approx Q_c Z_0 \left( \frac{1}{Q_1} + i \frac{2\Delta f}{f_r} \right) \quad (1)$$

where the right-hand side is valid near the resonance frequency,  $\Delta f = (f - f_r) \ll f_r$ . Here  $Q_c = Z_{\text{char}}/Z_0$  is the coupling quality factor,  $Q_1 = Z_{\text{char}}/R_{\text{eff}}$  is the internal quality factor and the characteristic impedance  $Z_{\text{char}} = \sqrt{L_0/C_{\text{eff}}}$ . We also define a loaded quality factor  $1/Q_L = (1/Q_c + 1/Q_1)$ .

# Article

The reflection coefficient of the resonator, measured by the reflectometry circuit, is given as:

$$\Gamma = \frac{Z - Z_0}{Z + Z_0} = 1 - \frac{2Q_L/Q_C}{1 + 2iQ_L(\Delta f/f_r)} \quad (2)$$

where the resonance frequency  $f_r = 1/\sqrt{L_0 C_{\text{eff}}} \approx f_{r0} (1 + 0.5L_K/(R_C^2 C_P))$  and  $f_{r0} = \sqrt{\frac{1}{L_0 C_P} - \frac{1}{R_C^2 C_P^2}}$ . In Supplementary Fig. 1c, we numerically evaluate the behaviour of the circuit with changing kinetic inductance, for  $L_0 = 205$  nH,  $C_P = 1.5$  pF and  $R_C = 3.5$  k $\Omega$ . These values are typical of a realistic experiment. We compare our analytical expression for  $f_r$  with the exact result and obtain a quantitative match for  $L_K \leq 500$  nH, the desired operation regime for our experiments, where the frequency shift is linearly related to the kinetic inductance, with  $\Delta f_r/f_{r0} = 1/(2R_C^2 C_P) \Delta L_K$ . In the normal state, the resonance frequency of the circuit is given as  $f_{r0} = \sqrt{\frac{1}{L_0 C_P} - \frac{1}{(R_C + R_n)^2 C_P^2}}$ , where  $R_n \approx 2 - 3$  k $\Omega$  is the normal-state channel resistance. Therefore, the loss of channel resistance near the transition from the normal to the superconducting regime results in a downshift of the resonance frequency  $f_{r0}$ .

## Circle fitting and analysis

Reflectometry measurement using a VNA provides the complex reflection coefficient  $S_{21}$  as a function of frequency. Apart from the ideal resonator response described in equation (2), two additional contributions appear in standard reflectometry measurements<sup>33</sup>. First, we account for an environmental factor:  $ae^{i(\alpha - 2\pi f\tau)}$ , representing an additional amplitude  $a$ , a phase shift  $\alpha$  and a cable delay  $\tau$  determined by the speed of light and the finite length (about 50 mm) of the coaxial cable connecting the device to the direction coupler mounted on the mixing chamber. Second, a phenomenological term  $\phi$  is introduced to account for the finite asymmetry of the resonances. This asymmetry is usually small and appears in the complex plane represented by  $\mathcal{R}(S_{21}) - \mathcal{J}(S_{21})$  as a rotation of the resonance circle along the real axis by an amount  $\phi$  (ref. 33).

$$S_{21} = ae^{i(\alpha - 2\pi f\tau)} \left[ 1 - \frac{2(Q_L/Q_C)e^{i\phi}}{1 + 2iQ_L(f/f_r - 1)} \right] \quad (3)$$

We fit our  $S_{21}$  data in the complex plane to equation (3) using the publicly available circle fitting package<sup>33</sup>. An example of the fitting in the complex plane is shown in Extended Data Fig. 3. The fit parameters  $f_r$ ,  $Q_L$  and  $Q_C$  are further analysed using the analytical model described in the RF resonator method section in Methods. In Supplementary Fig. 2, we show the analysis procedure for converting the resonance frequency into kinetic inductance and superfluid stiffness, as a function of temperature at a representative value of the filling factor  $\nu = -2.4$ . We can similarly perform a quality factor analysis using  $Q_L$  and  $Q_C$  and estimate the RF resistance ( $R_{\text{RF}}$ ) of the sample, using the relation  $R_{\text{RF}} = \frac{L_0}{Z_0 C_P} (Q_C/Q_L - 1)$ . At perfect matching,  $Q_L = Q_C/2$  such that  $R_{\text{RF}} = \frac{L_0}{Z_0 C_P}$ , the impedance-matching criterion we used to design our circuits. In Supplementary Fig. 3, we show this analysis as a function of  $T$  and  $\nu$ .  $R_{\text{RF}}(\nu, T)$  (Supplementary Fig. 3e) shows good qualitative agreement with both two-terminal resistance  $R_{2t}$  and four-terminal resistance  $R_{4t}$  (Supplementary Fig. 3c,d). In the superconducting state, when  $R_{4t} = 0$ , we obtain a quantitative match between  $R_{\text{RF}}$  and  $R_{2t}$  where  $R_{\text{RF}} \approx R_{2t} \approx R_c$  arises purely from the contact resistance  $R_c \approx 3.2$  k $\Omega$ .

## Superfluid stiffness phenomenology and main equations

Here we derive the formulas for superfluid stiffness of a nodal superconductor, used in the main text. For the temperature and current dependence, we focus on the effects of quasiparticles near the nodes. We note that the effects of classical phase fluctuations can also produce a linear-in- $T$  suppression of  $\rho_s$ . However, these are expected to

be suppressed below  $T_Q \approx \hbar R/L$ , which for our parameters ( $R \approx 1$  k $\Omega$ ,  $L \approx 100$  nH) yields about 500 mK (ref. 46).

We begin with a mean-field model for superconducting pairing in the active hole bands of TBG. There are two doped hole bands on top of the  $\nu = -2$  state. We assume these to be described by a single spin-degenerate band with singlet pairing, for simplicity and concreteness, although the formalism can be adapted to more general scenarios as well.

$$\begin{aligned} & \sum_{\mathbf{k}} \xi(\mathbf{k}) (c_{\mathbf{k},\uparrow}^\dagger c_{\mathbf{k},\uparrow} + c_{\mathbf{k},\downarrow}^\dagger c_{\mathbf{k},\downarrow}) \\ & + \Delta(\mathbf{k}) (c_{\mathbf{k}+\mathbf{Q}/2,\uparrow}^\dagger c_{-\mathbf{k}+\mathbf{Q}/2,\downarrow} + c_{-\mathbf{k}+\mathbf{Q}/2,\downarrow}^\dagger c_{\mathbf{k}+\mathbf{Q}/2,\uparrow}) \\ & = \sum_{\mathbf{k}} \begin{bmatrix} c_{\mathbf{k}+\mathbf{Q}/2,\uparrow}^\dagger \\ c_{-\mathbf{k}+\mathbf{Q}/2,\downarrow}^\dagger \end{bmatrix} \begin{bmatrix} \xi(\mathbf{k}+\mathbf{Q}/2) & \Delta(\mathbf{k}) \\ \Delta(\mathbf{k}) & -\xi(-\mathbf{k}+\mathbf{Q}/2) \end{bmatrix} \begin{bmatrix} c_{\mathbf{k}+\mathbf{Q}/2,\uparrow} \\ c_{-\mathbf{k}+\mathbf{Q}/2,\downarrow} \end{bmatrix} + \\ & + \sum_{\mathbf{k}} \xi(-\mathbf{k}+\mathbf{Q}/2), \end{aligned} \quad (4)$$

where  $\xi(\mathbf{k}) = \varepsilon(\mathbf{k}) - \mu$ , where  $\varepsilon(\mathbf{k})$  is the single-particle dispersion,  $\mu$  is the chemical potential,  $c^\dagger$  ( $c$ ) is the fermion creation (annihilation) operator. The momentum  $\mathbf{Q} = \mathbf{q}_0 + \mathbf{q}$  is the total momentum of the Cooper pair.  $\mathbf{q}_0$  is due to the static current driven through the system and  $\mathbf{q}$  describes the small deviations from the average current.

Although the last piece of equation (4) is a  $c$  number it still contributes to the total energy of the system and needs to be included to avoid convergence issues in the final expressions. It is noted that, in general,  $\Delta(\mathbf{k})$  can be dependent on  $\mathbf{Q}$  as well, but we ignore this dependence for simplicity. This assumption corresponds to neglecting the quantum geometric contribution to the stiffness<sup>47–49</sup>; see, for example, Appendix A2 of ref. 49 for a discussion in the projected context. We neglect the quantum geometric stiffness here because in generic models it depends on self-consistent energetics, and thus a microscopic model for the pairing, in addition to the active band wavefunctions<sup>48</sup>. In the case of the TBG bands, we expect the geometric contribution to have the same qualitative dependence on doping as the kinetic contribution, as the dominant kinetic contribution is itself ‘geometric’: it arises from interactions and the  $\mathbf{k}$  dependence of single-particle wavefunctions. We discuss this point further in Supplementary Information in the context of the band structure on top of the correlated insulator, where it has been shown that interband contributions to the stiffness vanish<sup>50</sup>. Our approximation takes into account the interaction-generated kinetic contribution to the stiffness, which makes the bands more dispersive than the bare ones, and only neglects the contributions coming from interactions between doped charges<sup>50–52</sup>, for which a theory of the superconducting ground state is necessary in general.

The superfluid stiffness can be obtained by expanding the grand potential  $\Omega$  in  $\mathbf{q}$ :  $[\rho_s]_{\alpha\beta} = \frac{1}{\hbar^2} \frac{\partial \Omega}{\partial q_\alpha \partial q_\beta} \bigg|_{\mathbf{q}=0}$  (refs. 47,48), where  $\alpha$  and  $\beta$  are indices in space ( $x, y$ ), or by calculating the current–current response. We note two convention differences from previous studies: a different definition of Cooper-pair momentum, as well as the computation of the superfluid stiffness instead of the superfluid weight  $D_s = 4\rho_s$ . These differences correspond to equal and opposite factors of four in the previous expression.

From equation (4) we obtain:

$$\begin{aligned} \Omega & \approx -T \sum_{\omega_n, \mathbf{k}} \text{Tr} \log [i\omega_n - \Delta(\mathbf{k}) \hat{\tau}_i \\ & - \{ \xi(\hat{\mathbf{k}}_0) \hat{\tau}_3 + \partial_\alpha \xi(\hat{\mathbf{k}}_0) q_\alpha / 2 + \partial_\alpha \partial_\beta \xi(\hat{\mathbf{k}}_0) \hat{\tau}_3 q_\alpha q_\beta / 8 \}] \\ & + \sum_{\mathbf{k}} \xi(\mathbf{k} + \mathbf{q}_0/2) + \partial_\alpha \xi(\mathbf{k} + \mathbf{q}_0/2) q_\alpha / 2 + \partial_\alpha \partial_\beta \xi(\mathbf{k} + \mathbf{q}_0/2) q_\alpha q_\beta / 8, \\ & \hat{\mathbf{k}}_0 = \mathbf{k} + \hat{\tau}_3 \mathbf{q}_0 / 2. \end{aligned} \quad (5)$$

where  $\tau_i$  are matrices in Gor’kov–Nambu space,  $\omega_n = (2n+1)\pi T$  is the fermionic Matsubara frequency ( $T$  being the temperature and  $n$  being non-zero integers), and we assume time reversal symmetry  $\xi(-\mathbf{k}) = \xi(\mathbf{k})$ .



The linear-in- $\mathbf{q}$  terms vanish after angle integration for  $\mathbf{q}_0 = 0$  but are non-zero otherwise, corresponding to a finite supercurrent. Although  $\xi(\mathbf{k})$  vanishes at the Fermi surface,  $\partial_\alpha \xi(\mathbf{k})$  and  $\partial_\alpha \partial_\beta \xi(\mathbf{k})$  in general do not. This allows us to take  $\mathbf{k} \pm \mathbf{q}_0/2 \approx \mathbf{k}$  in those derivatives and take  $\xi(\mathbf{k} \pm \mathbf{q}_0/2) \approx \xi(\mathbf{k}) \pm \mathbf{v} \cdot \mathbf{q}_0/2$ . Then we get:

$$\begin{aligned} [\rho_s]_{\alpha\beta} &= [\rho_s^{\text{dia}}]_{\alpha\beta} + [\rho_s^{\text{para}}]_{\alpha\beta}, \\ [\rho_s^{\text{dia}}]_{\alpha\beta} &= \frac{1}{4} \sum_{\mathbf{k}} \left\{ 1 + T \sum_{\omega_n} \text{Tr}[\hat{G}(i\omega_n, \mathbf{k}) \hat{\tau}_3] \right\} \partial_\alpha \partial_\beta \xi(\mathbf{k}) = \\ &= \frac{1}{4} \sum_{\mathbf{k}, \sigma} \langle c_{\mathbf{k}, \sigma}^\dagger c_{\mathbf{k}, \sigma} \rangle \partial_\alpha \partial_\beta \xi(\mathbf{k}) \\ &= \frac{1}{4} \sum_{\mathbf{k}} \left( 1 - \frac{\xi(\mathbf{k}) \tanh \left[ \frac{\sqrt{\xi^2(\mathbf{k}) + |\Delta(\mathbf{k})|^2}}{2T} \right]}{\sqrt{\xi^2(\mathbf{k}) + |\Delta(\mathbf{k})|^2}} \right) \partial_\alpha \partial_\beta \xi(\mathbf{k}) \\ [\rho_s^{\text{para}}]_{\alpha\beta} &= \frac{1}{4} T \sum_{\omega_n, \mathbf{k}} \text{Tr}[\hat{G}(i\omega_n, \mathbf{k}) \partial_\alpha \xi \hat{G}(i\omega_n, \mathbf{k}) \partial_\beta \xi], \end{aligned} \quad (6)$$

where

$$\hat{G}(i\omega_n, \mathbf{k}) = - \frac{i\omega_n - \mathbf{v} \cdot \mathbf{q}_0/2 + \xi \hat{\tau}_3 + \Delta(\mathbf{k}) \hat{\tau}_1}{[\omega_n + i(\mathbf{v} \cdot \mathbf{q}_0)/2]^2 + \xi^2 + \Delta^2(\mathbf{k})} \quad (7)$$

For  $\partial_\alpha \partial_\beta \xi(\mathbf{k}) = \text{constant}$  (such as for parabolic band),  $\rho_s^{\text{dia}}$  is simply proportional to the electron density, which is temperature independent. Ignoring corrections to the chemical potential (assuming  $T \ll E_F$ ), corrections to  $\rho_s^{\text{dia}}$  can arise from the vicinity of the nodes. However, the leading term will arise from the expansion  $\partial_\alpha \partial_\beta \xi(\mathbf{k}) \approx a_0 + a_1 \xi$ , so that the integral over momentum will take the form  $\int d\xi d\Delta \exp[-\sqrt{\xi^2 + \Delta^2}/2T] a_1 \xi^2 / \sqrt{\xi^2 + \Delta^2}$  and will scale as  $\propto T^3$  in temperature.

We thus focus on  $\rho_s^{\text{para}}$  and its temperature dependence. Evaluating the trace we get:

$$\begin{aligned} [\rho_s^{\text{para}}]_{\alpha\beta} &= \frac{T}{2} \sum_{\omega_n, \mathbf{k}} \frac{v_\alpha v_\beta}{([\omega_n + i(\mathbf{v} \cdot \mathbf{q}_0)/2]^2 + \xi^2 + \Delta^2(\mathbf{k}))^2} \\ &= - \frac{1}{16T} \sum_{\mathbf{k}} v_\alpha v_\beta \left( \frac{1}{\cosh^2 \frac{\sqrt{\xi^2 + \Delta^2(\mathbf{k}) + (\mathbf{v} \cdot \mathbf{q}_0)/2}}{2T}} \right. \\ &\quad \left. + \frac{1}{\cosh^2 \frac{\sqrt{\xi^2 + \Delta^2(\mathbf{k}) - (\mathbf{v} \cdot \mathbf{q}_0)/2}}{2T}} \right). \end{aligned} \quad (8)$$

As the contribution is exponentially suppressed by the gap, we focus on the vicinity of the nodes, where  $\Delta(\mathbf{k}) \approx \mathbf{v}_\Delta \cdot (\mathbf{k} - \mathbf{k}_F)$  and  $\xi \approx \mathbf{v} \cdot (\mathbf{k} - \mathbf{k}_F)$ .

$$\begin{aligned} \delta\rho_s(T, I)/1\text{node} &= [\rho_s^{\text{para}}]_{\alpha\beta} \\ &\approx \sum_n - \frac{v_n^\alpha v_n^\beta / (v_n v_\Delta)}{16T \sin\theta_{v, v_\Delta}} \int \frac{d\xi d\Delta}{(2\pi)^2} \left( \frac{1}{\cosh^2 \frac{\sqrt{\xi^2 + \Delta^2} + (\mathbf{v}_n \cdot \mathbf{q}_0)/2}{2T}} \right. \\ &\quad \left. + \frac{1}{\cosh^2 \frac{\sqrt{\xi^2 + \Delta^2} - (\mathbf{v}_n \cdot \mathbf{q}_0)/2}{2T}} \right) \\ &= - \sum_n \frac{v_n^\alpha v_n^\beta / (v_n v_\Delta)}{4\pi \sin\theta_{v, v_\Delta}} T \log \left[ 2 \cosh \frac{(\mathbf{v}_n \cdot \mathbf{q}_0)}{4T} \right], \end{aligned} \quad (9)$$

where  $\mathbf{q}_0 \propto \mathbf{I}$  (Supplementary equation 2). Thus, at zero current, one gets  $\delta\rho_s \propto -T$ , whereas at  $(\mathbf{v} \cdot \mathbf{q}_0) \gg T$  one gets  $\delta\rho_s \propto -I$ . It is noted that expression (9) can be modified by Fermi-liquid effects; these result in an additional multiplicative factor in the above formula<sup>3</sup>; in cuprates the value of this factor was found to be close to one<sup>53,54</sup>.

The results simplify considerably for: (1) symmetry-protected nodes, that is,  $\mathbf{v} \perp \mathbf{v}_\Delta$ , and (2) a non-nematic superconducting state, that is,  $\rho_{\alpha\beta} \propto \delta_{\alpha\beta}$ . From assumption 2, it follows that  $\sum_n (v_n^\alpha)^2 = Nv^2/2$ , where  $N$  is the number of nodes. For  $N = 4$  (d wave), we recover  $\delta\rho_s(T, q_0 = 0) = -\frac{v \log 2}{2\pi v_\Delta} T$  (ref. 1).

Let us now estimate how the current-induced correction depends on temperature. We use  $q_0 = \frac{I}{2e\rho_s^0 W}$  from Supplementary equation 2 and expand equation (9) using assumptions 1 and 2. We further compute the  $\rho_s \approx \text{Tr} \rho_{\alpha\beta}/2$  to average over current-induced anisotropies. The result is

$$\delta\rho_s(T \gg vq_0) = - \frac{Nv}{8\pi v_\Delta} T \left( \log 2 + \frac{v^2 I^2}{16(4e\rho_s^0 W)^2 T^2} \right) \quad (10)$$

Now let's express  $\delta\rho_s$  at large current (compared with the effects of temperature):

$$\delta\rho_s(vq_0 \gg T) = \frac{Nv^2}{64v_\Delta \pi e\rho_s^0 W} \langle \cos\theta_{I, v_n} \rangle \quad (11)$$

### Nodal quasiparticles

The quasiparticle contribution to the linear-in- $T$  suppression of  $\rho_s(T) \propto n_s(T) \propto n_s(0) - n_{\text{qp}}(T)$  implies a linear-in- $T$  increase in the quasiparticle density,  $n_{\text{qp}}$ . This is not expected in a fully gapped superconductor, where the quasiparticle population is exponentially suppressed for  $T \leq 0.3 T_c$ . Instead, it is consistent with a 2D nodal superconducting order, where the superconducting gap vanishes along certain directions—referred to as ‘nodes’—on the Fermi surface<sup>1,3</sup>, leading to a linear dispersion for the quasiparticle excitations. We illustrate this in Fig. 2c, inset, where we plot the superconducting quasiparticle energy dispersion near a node in the lattice momentum  $k$ -space. Two distinct velocities  $v_\Delta$ , corresponding to the slope of the superconducting gap, and  $v_F$ , the Fermi velocity describe the linear dispersion parallel and perpendicular to Fermi surface, respectively, forming an elliptic cone (see Supplementary Fig. 9 for a detailed description). A non-zero  $T$  would immediately populate this cone with an equal number of quasiparticles and quasiholes, with their density linearly proportional to  $T$ .

### BKT transition

In the BKT theory, for  $T > T_{\text{BKT}}$ , the phase coherence of a 2D superconductor is destroyed owing to the proliferation of unbound vortices, restoring a finite resistance owing to their dissipative motion. Experimentally, we can estimate the density-dependent BKT transition temperature from Fig. 3a by locating the temperature  $T_0$  where  $\rho_s(T, v)$  (smoothed for clarity) intersects with the universal  $\rho_c = 2T/\pi$  plane. As shown in the top panel of Fig. 3a, we find the  $T_0(v)$  is smaller than  $T_c$  obtained from the d.c. transport, indicating that the TTG device is superconducting even at  $T > T_0$ . This observation is rather surprising as the simple BKT model seems to break down. Although this observation could be explained by an unusually large vortex-core energy suppressing the proliferation of vortices  $T > T_{\text{BKT}}$  (refs. 55,56), we find an explanation associated with sample inhomogeneity more plausible, as discussed below.

It is known that superconductivity in MATMG samples suffers from twist-angle disorder<sup>35,36</sup>, which can create inhomogeneous superconductivity<sup>9–11</sup>, and percolation paths when a supercurrent flows in the sample. Given such a network of superconducting paths, as illustrated in Fig. 3b, inset, the aspect ratio of the device  $l/w$  for two-terminal d.c. and RF transport should be rescaled using the narrower effective sample width  $w^*$ . Therefore, our estimated  $\rho_s$  from the measured kinetic

response underestimates the true superfluid stiffness by a factor of  $\alpha = w/w^*$ . We can estimate  $\alpha$  from our experiment by noting the remarkable relationships between experimentally measured  $\rho_{s0}$ ,  $T_0$  and  $T_c$  as shown in Fig. 3b. In particular, we find  $T_c/T_0 \approx 3.0$  by taking the ratio between the slopes of the linear parts in  $T_c$  versus  $\rho_{s0}$  and in  $T_0$  versus  $\rho_{s0}$ . Considering  $T_{\text{BKT}} \approx T_c$  in MATMG<sup>10,11</sup> (that is, zero resistivity for  $T < T_{\text{BKT}}$ ), we estimate  $\alpha = w/w^* \approx T_{\text{BKT}}/T_0 \approx T_c/T_0 \approx 3.0$

## Theoretical $\rho_s$ from TTG band structure

We compare the experimental  $\rho_s(v)$  with the theoretical estimate. Starting at  $v = -2$ , the initial steep rise of  $\rho_s$  is enabled by a large positive band curvature  $\nabla_k^2 E$  near  $k = 0$ . However, on further doping,  $\nabla_k^2 E$  becomes negative, causing a reduction of the superfluid stiffness. Remarkably, the maximum of  $\rho_s$  is reached well below the half-filling of the band owing to its strong particle-hole asymmetry. Furthermore, taking into account the non-parabolic band dispersion in TTG shown in Fig. 3c, we estimate  $T_c/E_F \approx 0.03-0.08$ . This estimate is based on the linear slope between  $T_c$  and  $\rho_{s0}$ , and the calculated relationship between  $\rho_{s0}$  and  $E_F$  (Supplementary Fig. 8). We have observed similar linear scaling relationships for  $\rho_{s0}$  and  $T_c$  in other devices, in both electron- and hole-doped sectors, even when effects of twist-angle disorder are evident (Extended Data Fig. 4). This suggests the generality of this effect in MATMG superconductivity.

However, the theoretical estimates are larger than the experimental values by a factor of five, even after the geometrical factor correction by  $\alpha$ . This discrepancy suggests that only a fraction of the electronic spectral weight is condensed into the superfluid<sup>49-52,57</sup>. We leave the understanding of this to future studies. It is worth noting that a similar reduction of superfluid stiffness with increasing doping is observed in overdoped cuprates and remains a subject of active investigation<sup>39,58</sup>.

We note that the contribution from quantum geometry to  $\rho_s$  has been shown to be significant in attractive Hubbard models with flat-band electrons<sup>47,59-61</sup>. In our Hartree-Fock-based analysis presented here, the long-range Coulomb interactions are projected on to the flat bands taking the full form of the wavefunctions and their quantum geometric properties into account, which allows to capture both the symmetry-broken state and the finite superfluid stiffness at least qualitatively. A more thorough consideration of electron-electron interactions leading to both symmetry-broken states and superconductivity is required for a quantum geometry calculation of  $\rho_s$  and is left for future study. Finally, we note that TTG hosts a dispersive Dirac band in addition to the flat bands<sup>10</sup>. The contribution of the dispersive band towards  $\rho_s$  can be neglected as it provides a dissipative channel that is shorted out by the parallel superconducting channel originating from the flat bands.

## Estimates of the nonlinear Meissner effect

We model the electrodynamic response of a 2D nodal superconductor in the presence of a d.c. supercurrent bias (Methods), and obtain a quadratic dependence for  $I < I^*$ :

$$\Delta\rho_s(I) = -\frac{\nu_F^3}{\nu_\Delta} \frac{1}{T} \frac{N}{128(4e\rho_{s0}w^*)^2} I^2 \quad (12)$$

and a linear dependence for  $I > I^*$ ,

$$\Delta\rho_s(I) = -\frac{\nu_F^2}{\nu_\Delta} \frac{N \langle |\cos\theta_{I,\nu_F}| \rangle}{16(4e\rho_{s0}w^*)} I \quad (13)$$

with the crossover current  $I^*(T) = (2e\rho_{s0}w^*/\nu_F)T$  separating the quadratic and linear regimes of  $\rho_s(I)$ . Here  $\langle |\cos\theta_{I,\nu_F}| \rangle$  represents the angle between the applied supercurrent direction and the Fermi velocity at the node, averaged over all gap nodes.

We note that a simple picture of twist-angle inhomogeneity where superconducting islands are Josephson coupled through macroscopic

normal regions cannot explain the observed nonlinear Meissner effect and linear- $T$  variation of  $\rho_s(T)$ . However, more subtle forms of twist-angle disorder cannot be ruled out. See Supplementary Information section 4 for a detailed discussion.

Choosing  $N = 4$  and  $\langle |\cos\theta_{I,\nu_F}| \rangle = 0.7$ , we can estimate  $\nu_F$  and  $\nu_\Delta$  using equations (12) and (13), and  $b(v)$  and  $c(v)$  extracted from experiments (see Methods for details). The estimated results are shown in Fig. 4h, where  $\nu_F$  covers a range of  $(0.1-0.7) \times 10^5 \text{ m s}^{-1}$ , and  $\nu_\Delta$  covers a range of  $(0.2-0.5) \times 10^4 \text{ m s}^{-1}$ , roughly an order of magnitude smaller than  $\nu_F$ . Remarkably, the density-dependent ratio  $\nu_F/\nu_\Delta$  estimated here yields similar magnitude (about 5-20) and dependence on  $v$  to estimates in Fig. 3e, which was based on an independent analysis of  $\rho_s(T)$  measurements. An alternative way to estimate  $\nu_F$  is to use experimental  $\rho_{s0}(v)$  and the aforementioned expression  $\rho_s(v) = \frac{\nu_F(v)k_F(v)}{8\pi}$ . This approach produces a similar but slightly smaller  $\nu_F$  (about  $(0.1-0.2) \times 10^5 \text{ m s}^{-1}$ ), shown as the purple solid line in Fig. 4h.

## Data availability

Source data are provided with the paper. All other data that support the findings of this study are available from the corresponding authors upon reasonable request.

45. de Visser, P. J. et al. Evidence of a nonequilibrium distribution of quasiparticles in the microwave response of a superconducting aluminum resonator. *Phys. Rev. Lett.* **112**, 047004 (2014).
46. Turneaure, S. J., Lemberger, T. R. & Graybeal, J. M. Effect of thermal phase fluctuations on the superfluid density of two-dimensional superconducting films. *Phys. Rev. Lett.* **84**, 987-990 (2000).
47. Peotta, S. & Törmä, P. Superfluidity in topologically nontrivial flat bands. *Nat. Commun.* **6**, 8944 (2015).
48. Peotta, S., Huhtinen, K.-E. & Törmä, P. Quantum geometry in superfluidity and superconductivity. Preprint at <https://arxiv.org/abs/2308.08248> (2023).
49. Verma, N., Guerci, D. & Queiroz, R. Geometric stiffness in interlayer exciton condensates. *Phys. Rev. Lett.* **132**, 236001 (2023).
50. Mendez-Valderrama, J. F., Mao, D. & Chowdhury, D. Low-energy optical sum rule in moiré graphene. *Phys. Rev. Lett.* **133**, 196501 (2023).
51. Mao, D. & Chowdhury, D. Diamagnetic response and phase stiffness for interacting isolated narrow bands. *Proc. Natl Acad. Sci. USA* **120**, e2217816120 (2023).
52. Mao, D. & Chowdhury, D. Upper bounds on superconducting and excitonic phase stiffness for interacting isolated narrow bands. *Phys. Rev. B* **109**, 024507 (2024).
53. Ioffe, L. B. & Millis, A. J. d-wave superconductivity in doped Mott insulators. *J. Phys. Chem. Solids* **63**, 2259-2268 (2002).
54. Lee, P. A., Nagaosa, N. & Wen, X.-G. Doping a Mott insulator: physics of high-temperature superconductivity. *Rev. Mod. Phys.* **78**, 17-85 (2006).
55. Benfatto, L., Castellani, C. & Giamarchi, T. Kosterlitz-Thouless behavior in layered superconductors: the role of the vortex core energy. *Phys. Rev. Lett.* **98**, 117008 (2007).
56. Hetel, I., Lemberger, T. R. & Randeria, M. Quantum critical behaviour in the superfluid density of strongly underdoped ultrathin copper oxide films. *Nat. Phys.* **3**, 700-702 (2007).
57. Hazra, T., Verma, N. & Randeria, M. Upper bounds on the superfluid stiffness and superconducting  $T_c$ : applications to twisted-bilayer graphene and ultra-cold Fermi gases. *Phys. Rev. X* **9**, 031049 (2019).
58. Mahmood, F., He, X., Bozovic, I. & Armitage, N. P. Locating the missing superconducting electrons in the overdoped cuprates  $\text{La}_{2-x}\text{Sr}_x\text{CuO}_4$ . *Phys. Rev. Lett.* **122**, 027003 (2019).
59. Hu, X., Hyart, T., Pikulin, D. I. & Rossi, E. Geometric and conventional contribution to the superfluid weight in twisted bilayer graphene. *Phys. Rev. Lett.* **123**, 237002 (2019).
60. Törmä, P., Peotta, S. & Bernevig, B. A. Superconductivity, superfluidity and quantum geometry in twisted multilayer systems. *Nat. Rev. Phys.* **4**, 528-542 (2022).
61. Ganiev, O. K. & Yavdivov, B. Superfluid density and critical current density in superconducting cuprates with an extended d-wave pairing symmetry. *Eur. Phys. J. B* **94**, 116 (2021).

**Acknowledgements** We thank S. Kivelson and E. Berg for discussions. The major experimental work is supported by ARO MURI (W911NF-21-2-0147). P.K. and A.B. acknowledge support from the DOE (DE-SC0012260). M.K. is supported by the STC Center for Integrated Quantum Materials, NSF Grant number DMR-1231319. A.V., P.L. and P.A.V. are supported by a Simons Investigator grant (A.V.) and by NSF-DMR 2220703. P.A.V. acknowledges support by a Quantum-CT Quantum Regional Partnership Investments (QRPI) Award. K.C.F. thanks M. Randeria for her musings inspiring this research direction. A.Y. and M.E.W. are supported by the Quantum Science Center (QSC), a National Quantum Information Science Research Center of the US Department of Energy (DOE). A.Y. is also partly supported by the Gordon and Betty Moore Foundation through grant GBMF ID #12762. K.W. and T.T. acknowledge support from the JSPS KAKENHI (grant numbers 21H05233 and 23H02052) and World Premier International Research Center Initiative (WPI), MEXT, Japan. Nanofabrication was performed at the Center for Nanoscale Systems at Harvard, supported in part by an NSF NNIN award ECS- 00335765.

**Author contributions** A.B., Z.H., M.K., K.C.F. and P.K. conceived of the experiment. Z.H., I.P., J.M.P. and A.Z. fabricated the devices, A.B., Z.H., M.E.W. and M.K. conducted the measurements and analysed the data. P.L., P.A.V. and A.V. conducted the theoretical analysis. R.M.W., A.Y., P.J.-H, P.A.V., A.V., K.C.F. and P.K. supervised the project. All authors discussed and wrote the paper. K.W. and T.T. supplied hBN crystals.

**Competing interests** The authors declare no competing interests.

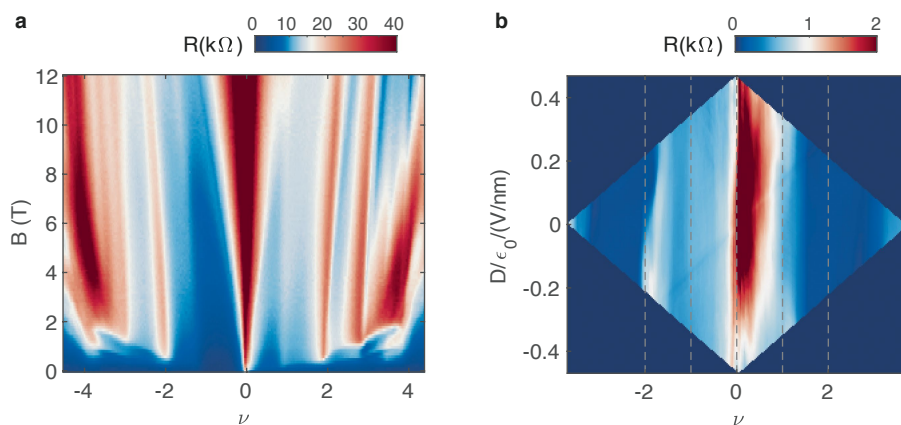
#### **Additional information**

**Supplementary information** The online version contains supplementary material available at <https://doi.org/10.1038/s41586-024-08444-3>.

**Correspondence and requests for materials** should be addressed to Kin Chung Fong or Philip Kim.

**Peer review information** *Nature* thanks Fan Zhang and the other, anonymous, reviewer(s) for their contribution to the peer review of this work. Peer reviewer reports are available.

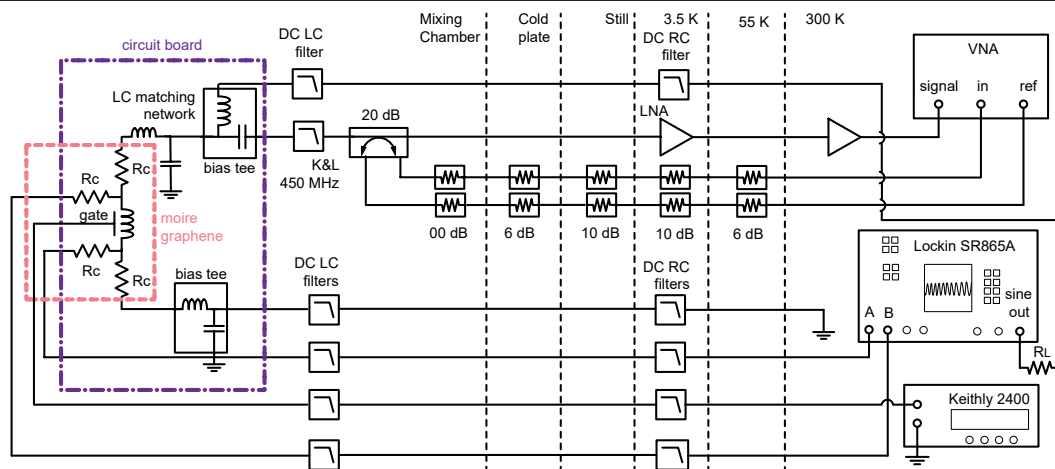
**Reprints and permissions information** is available at <http://www.nature.com/reprints>.



**Extended Data Fig. 1 | Device DC transport characterization. a**, TTG 4-terminal  $R$  as a function of  $\nu$  and magnetic field  $B$  at zero displacement field and a temperature of 2 K. The Landau fans show two set of structures: one set

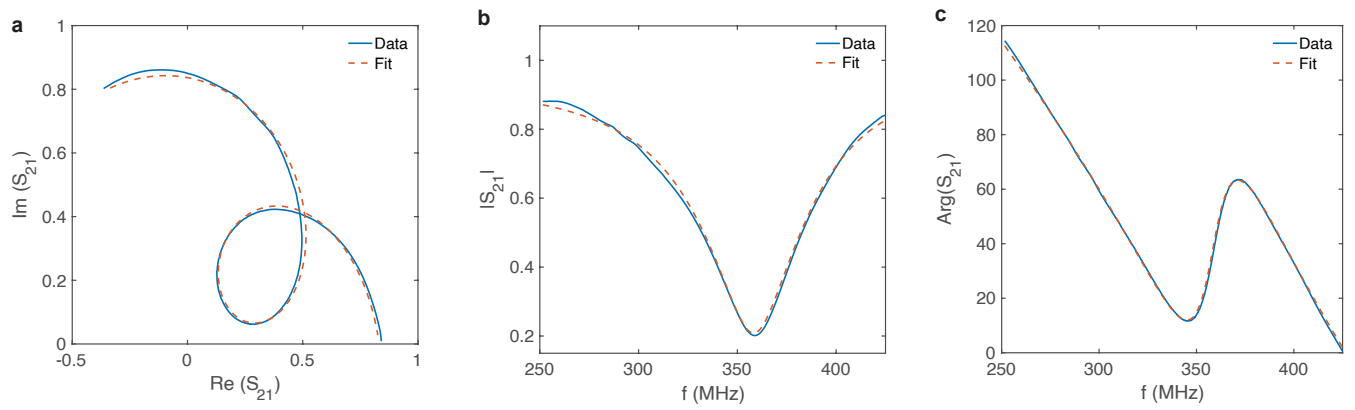
with large slopes and the other that appear at low  $B$  with shallow slopes. **b**, TTG 4-terminal  $R$  as a function of  $\nu$  and displacement field  $D$  at zero  $B$  and a temperature of 30 mK.



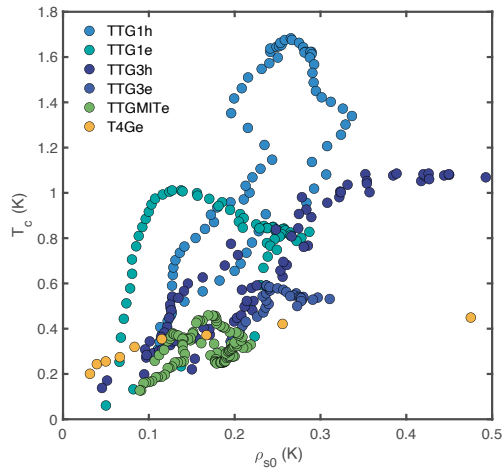


**Extended Data Fig. 2 | Measurement setup.** Circuit model of measurement setup for superfluid stiffness measurements. The moiré graphene sample is indicated by dashed pink lines while the circuit board—containing sample, LC matching network, and bias tees to allow impedance matching for microwave measurement—is indicated by dashed purple lines. DC and RF filtering is used

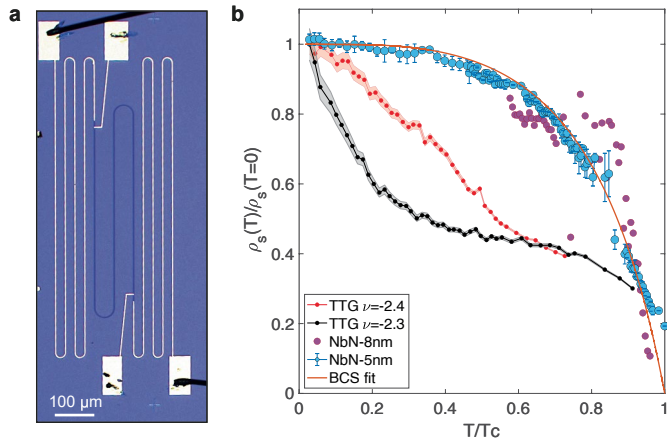
to reduce noise throughout the measurement chain. The RF signal is sent through an attenuated input line before entering a directional coupler. Sample contact resistance of  $\approx 3.2 \text{ k}\Omega$  is given by  $R_c$ . Graphite top and bottom gates are represented by “gate”. The final signal is amplified both at 4 K and room temperature before being measured by a vector network analyzer (VNA).



**Extended Data Fig. 3 | Circle fitting.** (a) Circle fitting of  $S_{21}$  in the complex plane. (b) Fitting of the reflection amplitude  $|S_{21}(f)|$ . (c) Fitting of the phase expressed in degrees  $\text{arg}(S_{21}(f))$ .



**Extended Data Fig. 4 | Uemura's law.** Scaling of  $\rho_{s0}$  versus  $T_c$  (obtained from resistance measurements) for both electron and hole side superconductors in all measured devices. A roughly linear trend is generally observed, even for devices with twist-angle disorder.



**Extended Data Fig. 5 | Superfluid stiffness in NbN thin films.** (a) Optical micrograph of a NbN thin film device with a meandering Au strip. The Au strip provides an additional resistance of 2.9 k $\Omega$  to mimic the contact resistance of TTG devices. We measured NbN samples thickness of 5 nm (NbN-5nm) and 8 nm (NbN-8nm) (b) Normalized superfluid stiffness  $\rho_s(T)/\rho_s(T=0)$  as a function of temperature  $T$  normalized with respect to the superconducting transition temperature  $T_c$  for TTG and NbN devices. TTG shows monotonically rising stiffness as the temperature is lowered, with a linear behavior for  $T/T_c \leq 0.3$ . On the other hand, the NbN devices show a robust saturation of the stiffness for  $T/T_c \leq 0.3$ . The NbN stiffness data obeys the BCS expectation. The BCS fit is given by  $\rho_s(T)/\rho_{s0} = \Delta(T)/\Delta_0 \tanh(\Delta(T)/T)$  where  $\Delta(T) = \Delta_0 \tanh(\pi T_c / \Delta_0 \sqrt{T_c/T - 1})$ ,  $\Delta_0 = 1.76 k_B T_c$ .